Applications of Orbital Imaging Radar for Geologic Studies in Arid Regions: The Saharan Testimony

Mohamed G. Abdelsalam, Cordula Robinson, Farouk El-Baz, and Robert J. Stern

Abstract

The multi-frequency and multi-polarization Shuttle Imaging Radar (SIR)-C/X Synthetic Aperture Radar (SAR) data collected in 1994 aboard two flights of the Shuttle Endeavour constitute a milestone in imaging of deserts from space. The data are here used to explore the eastern Sahara, including lithological and structural mapping, geomorphological studies, and mineral exploration. The SIR-C/X-SAR images in this environment are generally found to be (1) less useful for lithological mapping than orbital visible and near infrared (VNIR) images, except where rock types weather differently to produce varying roughness levels; (2) superior to orbital VNIR images for structural mapping in areas of subdued relief or where structures are partially covered by dry sand, as well as in tectonically active mountainous terrains; (3) superior to orbital VNIR images for mapping surface and sub-surface geomorphological features such as paleo-channels; and (4) useful in delineating geologic controls on mineral deposits, but inferior to orbital VNIR images for direct identification of these.

Introduction

Orbital imaging radar is unique in geologic remote sensing because it is an active system that uses signals with long wavelengths and systems with side-looking geometry. Radar bands used in orbital imaging systems lie in the microwave region of the electromagnetic spectrum and have wavelengths such as 3 cm for the X-band, 6 cm for the C-band, 10 cm for the S-band, and 24 cm for the L-band. The long wavelengths allow radar to have complete atmospheric transmission. The side-looking geometry of the system enhances imaging of low-lying relief. Topographic features show up most clearly at low radar look angles (Ford *et al.*, 1989). This allows an orbital radar system to image objects smaller than its spatial resolution cell. This makes radar of great importance in structural and geomorphological studies in the eastern Sahara. The long wavelengths, however, inhibit radar from measuring spectral features directly related to the mineralogy of geologic material; thus, it is of limited use in lithological mapping and mineral exploration compared to orbital visible and near infrared (VNIR) imaging systems. Orbital imaging radar, however, can be useful in lithological mapping and mineral exploration if different geologic materials have surface expressions in the form of distinctive roughness levels.

Another consequence of the long wavelengths is that radar can penetrate dry sand and collect images of shallow sub-surface features in arid regions such as the eastern Sahara. The arid climate prevents development of extensive soil and vegetation cover which otherwise obscures the returning radar signal from geologic features. Furthermore, the absence of moisture maximizes the depth of radar penetration in the well-sorted sand cover and enables imaging of shallow (up to 2 m) sub-surface features.

This presentation discusses the importance of orbital imaging radar in geologic studies in arid regions based on our experience in the eastern Sahara of North Africa. First, we outline the evolution of orbital imaging radar systems and summarize concepts that are important in understanding and interpreting radar images. Then, we discuss application of the Shuttle Imaging Radar (SIR) C/X Synthetic Aperture Radar (SAR) data to lithological and structural mapping, geomorphological studies and mineral exploration.

Orbital Imaging Radar Systems and SIR-C/X-SAR Data

The history of orbital imaging radar goes back to 28 June 1978 when the National Aeronautics and Space Administration (NASA) launched SEASAT, the first Earth-orbiting satellite designed for remote sensing of the oceans (Born *et al.*, 1979; Elachi, 1981; Fu and Holt, 1982). It carried the first spaceborne synthetic aperture radar (SAR) system. SEASAT lasted for 105 days before a short circuit ended the mission on 10 October 1978 (Table 1). SEASAT was followed in 1981 by the first shuttle imaging radar (SIR-A) system (Cimino and Elachi, 1982; Ford *et al.*, 1983)(Table 1). The experiment was a success in the eastern Sahara because SIR-A images revealed paleo-channels in northern Sudan and southern Egypt buried under the sand and not visible with VNIR images (McCauley *et al.*, 1982). SIR-B (Kobrick, 1985; Elachi, 1986; Ford *et al.*, 1986) (Table 1) followed shortly in 1984 and was advanced in that the data were digitally recorded, unlike SIR-A data which were optically recorded.

The early 1990s witnessed significant contributions in orbital imaging radar from the international community outside the U.S.A. The Russian Space Agency (PKA = RSA) launched in 1991 the Earth-orbiting satellite ALMAZ-1 (Yelizavetin, 1992) (Table 1). In that same year the European Space Agency (ESA) launched the Earth Remote Sensing Satellite (ERS)-1 (Schreier *et al.*, 1991; Koopmans, 1991; Askene *et al.*, 1992) (Table 1). ERS-2 was launched in 1995 to collect radar data similar to that of ERS-1 (Femenias-Pierre, 1998) (Table 1). In

M.G. Abdelsalam and R.J. Stern are with the Center for Lithospheric Studies, The University of Texas at Dallas, Richardson, TX 75080 (abdels@utdallas.edu).

C. Robinson and F. El-Baz are with the Center for Remote Sensing, Boston University, Boston, MA 02215.

TABLE 1: COMPARISON BETWEEN PAST, PRESENT, AND FUTURE ORBITAL IMAGING RADAR SYSTEMS

	SEA-SAT	SIR-A	SIR-B	ALMAZ-1	ERS-1	JERS-1	SIR-C	X-SAR	ERS-2	RADAR-SAT	PRIR-ODA	ENVI-SAT	SRTM	PAL-SAR	Light-SAR
Band	L	L	L	S	C	L	C,L	X	C	C	S,L	C	C	L	L
Polarization	HH	HH	HH	HH	VV	HH	All	VV	VV	HH	HH	All	HH	HH or VV HV or VH	All
Incident Angle (°)	23	45	20-60	30-60	24	35	17-60	17-60	24	17-50	35	20-45	20-60	20-55	20
Resolution (meter)	25	30	30	15	25	18	25	25	25	10-100	30	30	30	10-100	25-100
Swath Width (km)	100	50	50	20-45	100	76	15-100	15-40	100	50-170	120	50-400	60	70-250	50-500
Orbital Platform	Satellite	Space Shuttle	Space Shuttle	Satellite	Satellite	Satellite	Space Shuttle	Space Shuttle	Satellite	Satellite	Space Station	Satellite	Space Shuttle	Satellite	Satellite
Organization	NASA	NASA	NASA	RSA (PKA)	ESA	NSDA/MITI	NASA	DLR/ASI	ESA	CSA	RSA/DLR	ESA	NIMA/NASA/DLR/ASI	NASDA/MITI	NASA
Altitude (km)	790	225	225	300	790	568	225	225	785	790	394	800	233	700	790
Orbit Inclination (°)	108	57	57	72.7	97.7	97.7	57	57	97.7	98.6	51.6	100	57	98	97.7
Launch Date	1978	1981	1984	1991	1991	1992	1994	1994	1995	1995	1995	1998	2000	2002	2003
Life Time	105 days	11 days	11 days	2.5 y	3 y	2 y	11 days	11 days	3 y	5 y	2 y	5 y	11 days	3-5 y	3-5 y

Wavelengths are 3 cm for X band, 6 cm for C Band, 10 cm for S Band, and 24 cm for L Band. Polarizations are abbreviated as HH = Horizontally Transmitted and Horizontally Received, HV = Horizontally Transmitted and Vertically Received, VV = Vertically Transmitted and Vertically Received, and VH = Vertically Transmitted and Horizontally Received. Organization abbreviations are NASA = U.S. National Aeronautics and Space Administration, RSA (PKA) = Russian Space Agency, ESA = European Space Agency, NASDA = National Space Development Agency of Japan, MITI = Ministry of International Trade and Industry of Japan, DLR = Deutsches Zentrum Für Luft- und Raumfahrt or German Aerospace Center, ASI = Agenzia Spaziale Italiana or Italian Space Agency, and NIMA = U.S. National Imaging and Mapping Agency.

1992 the National Space Development Agency (NASDA) of Japan launched the Japanese Earth Resources Satellite (JERS)-1 (Moon *et al.*, 1994) (Table 1).

In 1994 NASA twice launched the Shuttle Endeavour to collect the first multi-spectral and multi-polarization SIR-C/X-SAR data between latitudes 57°N and 57°S. These data were collected with multi-look angles and swaths ranging in width between 15 and 100 km for the L and C bands and 15 and 40 km for the X band (Table 1). SIR-C/X-SAR data are advanced compared to SIR-A and SIR-B and other orbital radar data in that they were simultaneously collected at three wavelengths and multiple polarizations (Table 1). L and C bands were collected with like-polarization HH (horizontally transmitted and horizontally received) and VV (vertically transmitted and vertically received), and cross-polarization HV (horizontally transmitted and vertically received) and VH (vertically transmitted and horizontally received). X band was collected with VV only (Table 1).

The Canadian Space Agency (CSA) in 1995 put into orbit the first commercial imaging radar satellite RADARSAT (Parashar *et al.*, 1993) (Table 1). The PKA attached to MIR in the same year the first space station-borne radar system enclosed in the module PRIRODA of the German Aerospace Center (DLR = DAS).

NASA launched the Shuttle Radar Topography Mission (SRTM) in early 2000 (Farr and Kobrick, 1998; Okonek, 1999) (Table 1) to collect single-path, but repeated-take, data for interferometric uses between latitudes 60°N and 54°S. NASA also plans to utilize radar interferometry in measuring large-scale surface changes. For this purpose, the Lightweight Synthetic Aperture Radar (LightSAR) satellite mission is planned for the year 2003 (Schoonmaker, 1997; Evans and Moghaddam, 1998) (Table 1). Other future plans for orbital imaging radar include ESA ENVISAT1 (European Space Agency, 1998) (Table 1) and NASDA of Japan PALSAR satellite (NASDA, 1999).

Imaging with Orbital Radar

Orbital imaging radar systems depend on measuring the amplitude, time delay, and phase shifts of returned radar signals. Radar signals are produced by a source antenna with a side-looking geometry and measured by a receiving antenna after backscattering or volume-scattering off a surface (Zebker and Goldstein, 1986). The amplitude of the returned radar signal depends on system-related (wavelength, polarization, and incidence angle) and environment-related (surface and sub-surface roughness, slope, and dielectric properties) factors (Lewis *et al.*, 1998). These factors control three types of interaction between radar signals and the imaged surface (Lewis *et al.*, 1998): (1) reflection, (2) back-scattering, and (3) volume-scattering (Figure 1A).

Reflection

Reflection occurs when a radar signal encounters a smooth flat surface. The signal reflects away from the receiving antenna with an angle equals to that of the incident angle (Figure 1A). In this case no returning radar signal will be detected in the receiving antenna; hence smooth, flat surfaces appear dark on radar images.

Backscattering

Backscattering occurs when the radar signal encounters a rough surface. The radar waves scatter in different directions and some return to the receiving antenna (Figure 1A). Backscattering depends on the roughness level relative to the radar band wavelength. Shorter wavelengths increase the perceived surface roughness (Campbell and Campbell, 1992). Generally, a surface is considered rough if the weathering cell (roughness characteristics) equals or is greater than 10 percent of the radar band wavelength (Lewis *et al.*, 1998). In addition, at a constant wavelength, a flat surface is perceived as smoother as the look angle increases (Ford *et al.*, 1989).

Volume-Scattering

The term volume-scattering is used here to describe a returned radar signal that follows a path with more than one direction (Figure 1B). The two types of volume scattering are double-bounce and penetration (Figure 1A). Double-bounce is discussed together with normal-reflection (when the incident angle equals 90°, the path of the returning signal coincides with that of the incoming signal but is in the opposite direction) and edge-effect because they are all associated (Figure 1B).
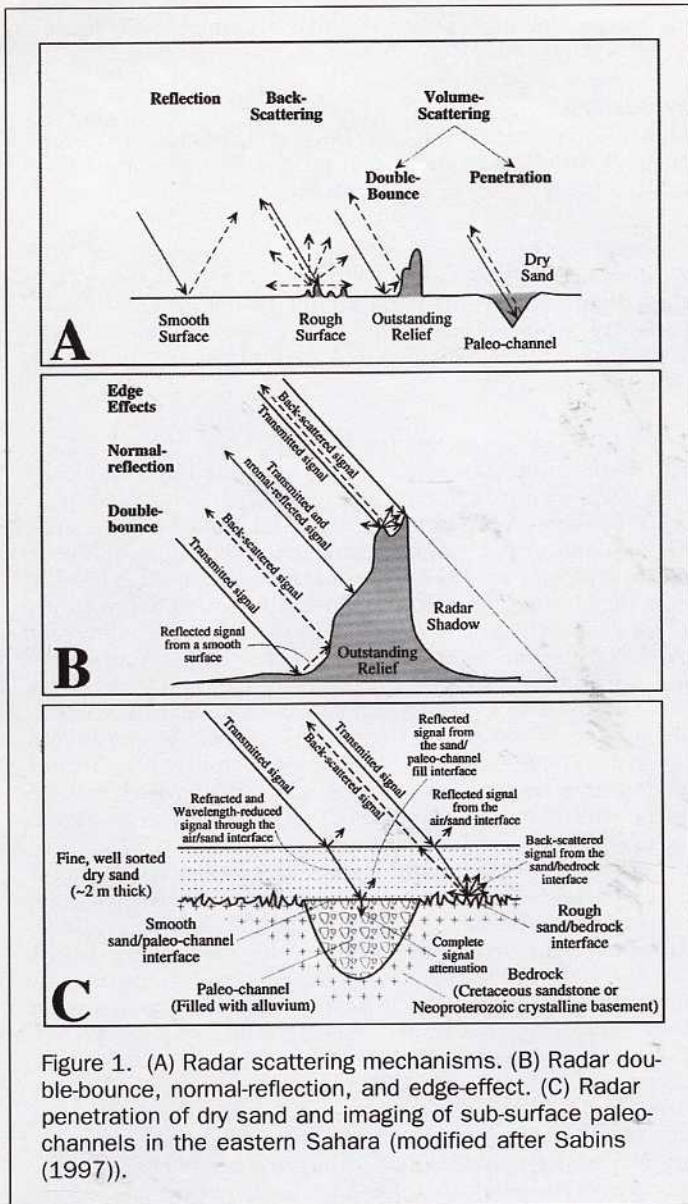
Figure 1. (A) Radar scattering mechanisms. (B) Radar double-bounce, normal-reflection, and edge-effect. (C) Radar penetration of dry sand and imaging of sub-surface paleo-channels in the eastern Sahara (modified after Sabins (1997)).

Lewis *et al.*, 1998) (Figure 1C). The optimum conditions for sub-surface imaging with orbital radar in arid regions are (1) smooth surface of fine-grained and well-sorted sand (Roth and Elachi, 1975) (Figure 1C); (2) very dry conditions (less than 1 percent moisture content) to minimize electrical conductivity and facilitate greater radar signal penetration (Campbell and Ulrichas, 1969; Hoekstra and Delaney, 1974); (3) limited depth of sand cover (Figure 1C); experiments show that a radar signal is attenuated to 37 percent at the air/sand interface and completely attenuated at depth of more than 2 meters at 1 percent moisture content (Elachi and Granger, 1982); (4) sub-surface imaging occurs when a rough sand/bedrock interface produces strong backscattering (Elachi *et al.*, 1984) (Figure 1C); and (5) in addition to the above environment-related factors, system-related factors important in optimizing radar penetration are (a) longer wavelengths result in deeper radar penetration (Schaber *et al.*, 1997) (Figures 2A, 2B, and 2C); (b) cross-polarization enhances radar penetration (Schaber *et al.*, 1997); and (c) sub-surface features are more likely to be revealed at radar look angles greater than 30° (Elachi *et al.*, 1984).
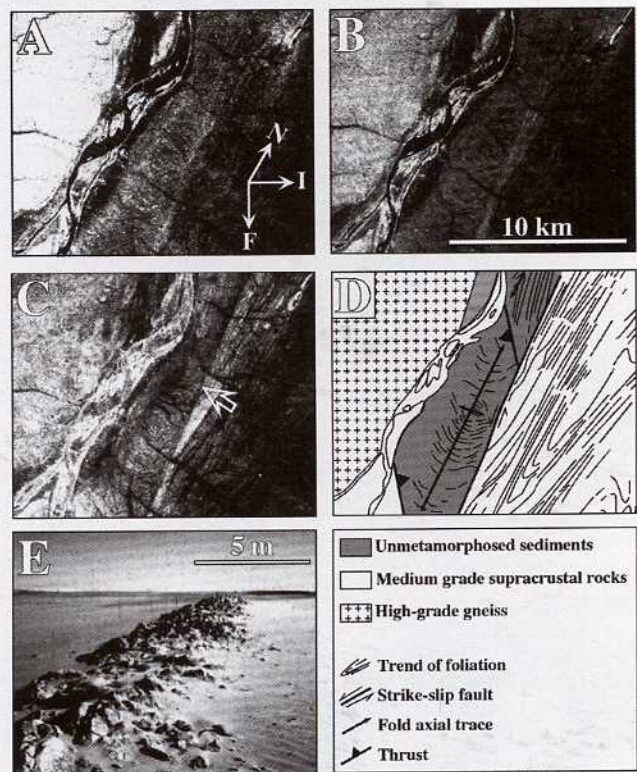

Figure 2. Images of part of the Neoproterozoic Keraf suture in northern Sudan. For location, see Plate 1. (A) X-VV image. (B) C-HH image. (C) L-HH image. (D) Lithologic and structural interpretation of the L-HH image. (E) A field photograph of a ~5 m wide ridge defining a mylonite zone associated with a sinistral shear zone in the Neoproterozoic Keraf suture. (B), (C), and (D) indicate greater depth of penetration with increasing wavelength. The L-HH image in 2C shows the shear zones because of the edge-effect caused by the narrow ridge in 2E shown by an open white arrow in 2C. This allows radar to image the ridge although it is smaller than its 30-m spatial resolution. The abbreviations in the arrows indicate north (N), radar illumination direction (I), and shuttle flight direction (F).

Double-Bounce, Normal-Reflection, and Edge-Effect

Double-bounce occurs when the radar signal reflects from a smooth flat surface, encounters outstanding relief, and is reflected back again to the receiving antenna (Figure 1B). Outstanding relief with a surface tilted nearly perpendicular to the radar signal results in normal-reflection (Figure 1B). Outstanding objects can also cause preferential backscattering from their edges and corners (Figure 1B). This is referred to as edge-effect and corner reflectors (Ford *et al.*, 1989). Double-bounce, normal-reflection, and edge-effect result in radar illumination/shadow where bright stripes are in juxtaposition with dark stripes.

Penetration

One of the most important characteristics of radar in geologic studies of the eastern Sahara is its ability to penetrate dry sand and image the shallow sub-surface features (Roth and Elachi, 1975; McCauley *et al.*, 1982; McCauley *et al.*, 1986; Elachi *et al.*, 1984; Blom *et al.*, 1984; Schaber *et al.*, 1997; Sabins, 1997;

Geomorphology of the Eastern Sahara

The eastern Sahara is dominated by three physiographic provinces (Plate 1): (1) the Red Sea Hills province, (2) the western margin of the Red Sea Hills province, and (3) the sand sheets and sand dune field province.

The Red Sea Hills province (Plate 1) is underlain by Neoproterozoic rocks of the Nubian Shield. This province extends south from the Gulf of Suez in Egypt to the Gulf of Zula in Eritrea (Plate 1). Further south, sedimentary and volcanic rocks of the Afar Depression overlay the Neoproterozoic rocks (Figure 3). The Red Sea Hills have rugged relief dominated by closely spaced mountain ranges that rise several hundred meters above the surrounding plain (Plate 1).

The western margin of the Red Sea Hills province occupies the area around the Nile in northern Sudan and Egypt (Plate 1). Low-lying outcrops that are partially covered by sand dominate the province. In northern Sudan this is a 100-km wide, 400-m above sea level, lower Tertiary to Recent peneplain (Sandford, 1949) described by Raisz (1952) as "Rock, sand, and gravel flats with few inselbergs and traces of dendritic river courses." The 500-km long, 50-km wide Neoproterozoic supracrustal passive margin deposits of the Keraf suture coincide with this province in northern Sudan (Abdelsalam et al., 1995; Abdelsalam et al., 1998; Abdelsalam and Stern, 1996). Basement outcrops are scarce and typically trap windblown sand. West of the Nile in the Bayuda Desert (Plat 1), the Nile Craton is an area of well-exposed low-lying outcrops of amphibolite-facies gneiss and supracrustal rocks. The relatively good exposure of basement rocks is due largely to trapping of south-migrating aeolian sand sheets by the Nile as it runs SW from Abu Hamed (Plate 1) and late Cenozoic uplift, which is expressed by scattered alkalic volcanic centers that range in age from mid-Miocene to Pleistocene (Barth et al., 1983).

The extensive sand sheets and sand dune fields province cover the area west of the Nile in northern Sudan and Egypt and west of the Bayuda Desert (Plate 1). It is occasionally disrupted by plateau of Cretaceous sandstone and Paleogene limestone.

Five outcrop types are recognized in the eastern Sahara, (1) mountainous, (2) inselbergs, (3) undulating basement plain with low-lying outcrops, (4) low-lying outcrops partially covered by sand, and (5) plains covered by sand sheets and sand dunes. These types are sometimes associated with distinct lithologies and might define regional structures with characteristics tones and textures in the SIR-C/X-SAR images.

Applications

The following sections discuss the application of SIR-C/X-SAR images to lithological and structural mapping, geomorphological studies, and mineral exploration.

Lithological Mapping

We have used SIR-C/X-SAR images to (1) map lithologic units in areas dominated by low-lying subdued relief using the Neoproteozoic Keraf suture in the Sudan as an example, and (2) remotely sense volcanic flows of the Erta Ale volcano in Ethiopia.

Areas with Low-Lying Subdued Relief

The Keraf suture in northern Sudan is defined by a 500-km long, 50-km wide, N-trending structural belt, which deforms passive margin supra-crustal rocks (Abdelsalam et al., 1995; Abdelsalam et al., 1998; Abdelsalam and Stern, 1996). The suture separates the Neoproterozoic Nubian Shield in the east from the Mesoproterozoic and older Nile Craton to the west and is defined by low-lying outcrops partially covered by sand (Abdelsalam et al., 1995; Abdelsalam et al., 1998; Abdelsalam and Stern, 1996). Owing to the sand cover, orbital VNIR images are of limited use, but SIR-A and SIR-C/X-SAR images are useful in mapping the Keraf suture (Abdelsalam et al., 1995; Abdelsalam et al., 1998; Abdelsalam and Stern, 1996). This is attributed to radar penetration as well as edge-effect, which enhance the imaging of low-lying outcrops that are smaller than the spatial resolution cell of both systems.

High-grade gneiss in the Bayuda Desert, west of the Keraf suture, forms low-lying, rough, and hilly terrain. Areas underlain by these rocks appear on the SIR-C/X-SARimage as diffuse dark and bright tones with no discernable pattern (Figure 2C). On the other hand, paragneiss intercalated with carbonates and amphibolites lying east of the Keraf suture form subdued areas defined by differentially eroded layers with sharp local relief. These appear as a succession of dark and bright bands on the SIR-C/X-SAR image (Figure 2C). Unmetamorphosed but deformed syn-tectonic sediments also exhibit this pattern on the SIR-C/X-SAR image (Figure 2C). However, fold geometry, spacing, continuity, and thickness of dark and bright bands in the SIR-C/X-SAR image enable differentiation between layered metamorphic assemblages and bedded unmetamorphosed, but deformed, sediments (Figures 2C and 2D).

Volcanic Flows

The Erta Ale is a shield volcano representing one of the axial ranges of the Afar Depression in northern Ethiopia (Plate 1 and Figure 3). The volcano is 80 km long, has a 40 km maximum width, and covers an area of 2350 km² (Berberi et al., 1972) (Figure 3). It is remote and rarely visited although it is known to have an active lava lake in its summit crater, and has been erupting continuously since 1967 (Oppenheimer and Francis, 1998)

Rocks in the Erta Ale volcano range in composition from mafic to felsic (Barrat et al., 1998). Berberi et al. (1972) mapped the volcano and idenified six rock types related to different eruption phases as indicated by several volcanic centers aligned NNW. SIR-C/X-SAR image of the Erta Ale volcano shows good correlation with the Berberi et al. (1972) map. Early submarine to sub-lacustrine mafic lava flows in the eastern part of the volcano show up in the radar image as darker than the rest of the volcano (Figure 3A). On the other hand, intermediate and felsic flows-including basal hawaiite, middle trachyte, and upper rhyolite and constituting the top part of the volcano-are very bright (Figure 3A). A significant difference between SIR-C/
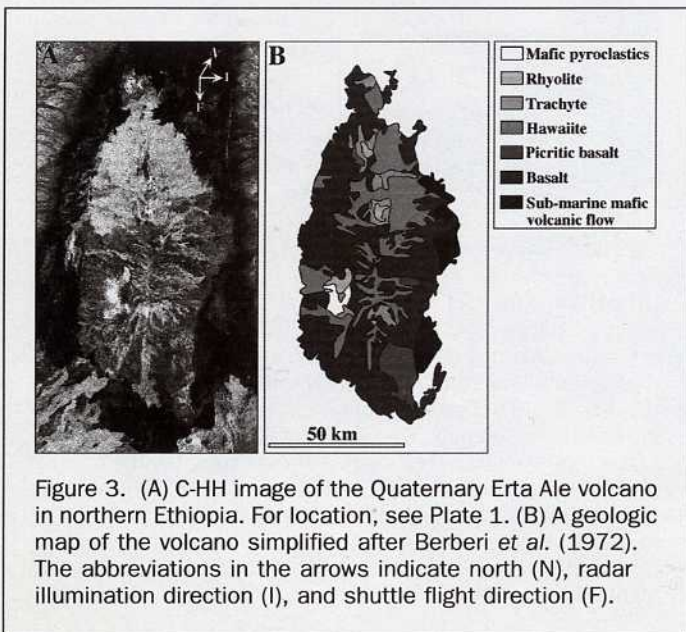

Figure 3. (A) C-HH image of the Quaternary Erta Ale volcano in northern Ethiopia. For location, see Plate 1. (B) A geologic map of the volcano simplified after Berberi et al. (1972). The abbreviations in the arrows indicate north (N), radar illumination direction (I), and shuttle flight direction (F).

Legend (Figure 3B):
- Mafic pyroclastics
- Rhyolite
- Trachyte
- Hawaiite
- Picritic basalt
- Basalt
- Sub-marine mafic volcanic flow

50 km

X-SAR image and the geologic map is that the radar image suggests that the intermediate to felsic flows are more extensive in the northern part of the volcano than the map indicates (Figure 3). The brightest part of the image corresponds to local mafic pyroclastic flow on the southwestern part of the volcano (Figure 3). Basaltic flows and picritic basaltic spatter cones comprise the majority of the shield volcano; these appear pale gray and are distinct from the dark gray representing the lower volcanic flow (Figure 3)

Structural Mapping
We have used SIR-C/X-SAR images to (1) map lithologically defined structure using the Neoproterozoic Keraf suture in northern Sudan as an example, and to (2) show morphologically defined structures as exemplified by the 20 Ma and younger normal faults of the Afar Depression in Ethiopia.

Lithologically Defined Structures
Structural features on the SIR-C/X-SAR images of the Keraf suture are defined by trends of alternating dark and bright bands which correspond to transposed bedding and metamorphic layering (Abdelsalam et al., 1995; Abdelsalam et al., 1998; Abdelsalam and Stern, 1996) (Figure 2C). Fold closures are defined by curvatures in these bands (Figure 2C). The planar view geometry of fold hinge zones (angular, rounded, or box) is well-defined on the SIR-C/X-SAR images. However, determining the three-dimensional geometry of folds (plunge of hinge line, attitude of the axial surface, and attitude of the limbs) is not possible based on the image alone. The structures of the Keraf suture are too low-lying for dip direction to be obtained from radar illumination/shadow.

Near-vertical faults in the Keraf suture appear as sharp, linear features in the SIR-C/X-SAR images (Figure 2C). This corresponds to a narrow (~5-m wide) ridges of mylonitized granite (Figure 2E) but is clearly imaged by SIR-C/X-SAR data (Figure 2D). Strike-slip faults mark sharp boundaries, the planar fabric on either side is either sharply truncated or sheared off (Abdelsalam et al., 1995; Abdelsalam et al., 1998; Abdelsalam and Stern, 1996) (Figure 2D).

Morphologically-Defined Structures
The Afar Depression has a well-developed topographic expression where 20 Ma and younger volcanic and tectonic features are associated with on-land "seafloor spreading" (Berberi et al., 1972; Berckhemer et al., 1975; Hayward and Ebinger, 1996) (Plate 1). The triangular-shaped, 200,000-km² depression extends south from the Gulf of Zula in Eritrea to the Main Ethiopian Rift (Plate 1). The Afar Depression is situated at the complex Red Sea - Gulf of Aden - Main Ethiopian Rift ridge-ridge-ridge triple junction above a mantle plume that has been inferred from geochemical and geophysical data (McKenzie et al., 1970; Mohr, 1983). NW-trending, normal-slip faults parallel to the Red Sea trend are defined by an obvious, west-facing fault escarpment (Hayward and Ebinger, 1996). SIR-C/X-SAR images with an easterly look direction show these faults with a series of radar illumination/shadows due to double-bounce, normal-reflection, and edge-effect (Figure 4). Hayward and Ebinger (1996) used Landsat TM images to trace faults in the Afar Depression, but found that it is difficult to locate those which are less than 1 km long and have surface expression of less than 30 m. They concluded that many important relationships between structural trends are overlooked because of the spatial limitation of Landsat TM data. However, faults with surface expression smaller than the spatial resolution cell of the SIR-C/X-SAR system can be located from these images (Figure 4).

Geomorphological Mapping
We discuss geomorphological mapping with SIR-C/X-SAR images as applied to (1) ground-water exploration and (2) understanding the evolution of the Nile in Nubia.
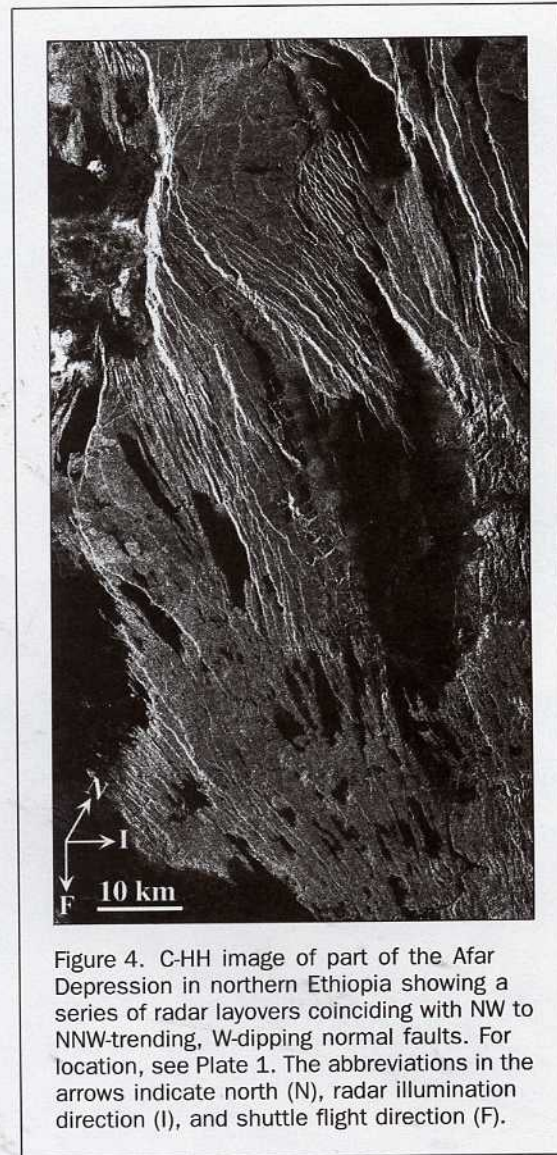

Figure 4. C-HH image of part of the Afar Depression in northern Ethiopia showing a series of radar layovers coinciding with NW to NNW-trending, W-dipping normal faults. For location, see Plate 1. The abbreviations in the arrows indicate north (N), radar illumination direction (I), and shuttle flight direction (F).

Ground-Water Exploration
SIR-A and SIR-C/X-SAR images reveal a number of paleo-drainage systems in the eastern Sahara. Dry channels constituting these drainage systems are referred to as radar rivers and are believed to be relicts from Tertiary (McCauley et al., 1982) to Pleistocene (Szabo et al., 1995) drainage systems and might represent part of the so-called Trans-African Drainage System (McCauley et al., 1982). Older and wider radar rivers were formed during the Tertiary, probably when the running surface water was exceedingly high (McCauley et al., 1982). This created radar rivers with wide peneplained valley floors. Running surface water in the eastern Sahara might have been scarce during late-Tertiary times but significantly increased during the Pleistocene (Szabo et al., 1995). This resulted in the formation of systems of braided rivers within the wider Tertiary valley floors (McCauley et al., 1982; Szabo et al., 1995).

Radar river morphologies and their distribution can be used to infer paleo-flow direction. Geomorphological studies in the eastern Sahara suggests that the paleo-flow direction was generally towards depressions such as the Kharga in the Great Salima Sand Sheet (Robinson et al., in press) and the Great Sand Sea (Plate 1; Figure 5). These depressions were probably
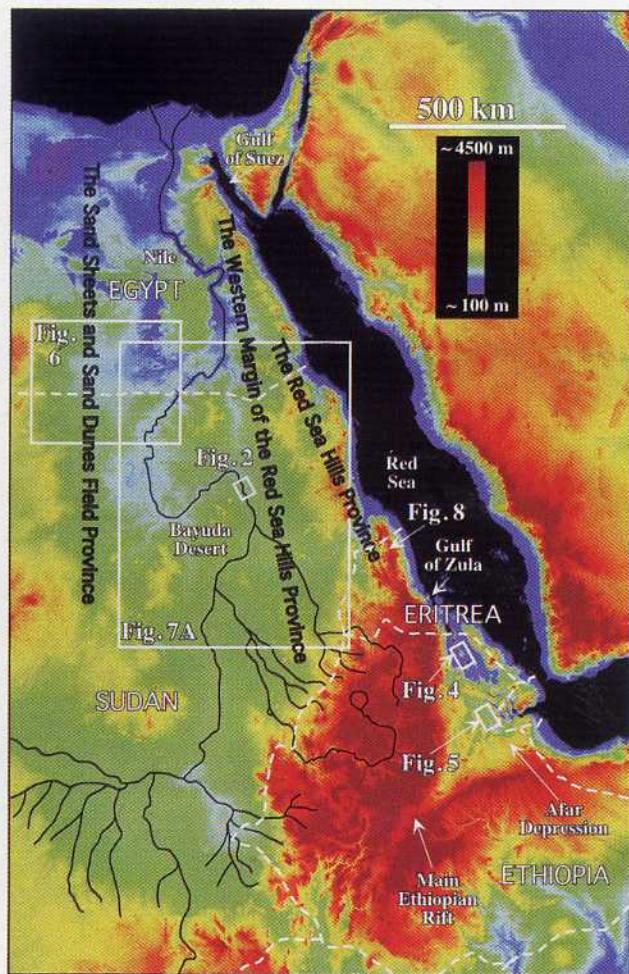
Plate 1. Digital elevation map of the eastern Sahara derived from the USGS global 30 arc seconds (1 km) elevation data set (GTOPO30).
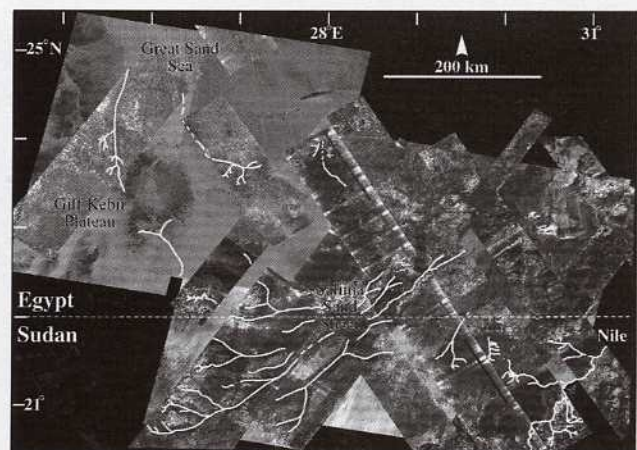

Figure 5. An L-HH mosaic showing paleo-drainage in northern Sudan and southern Egypt. For location, see Plate 1. The distribution of the paleo-drainage (drainage is shown by white lines) suggests that it was flowing towards the land-locked depression of the Salima Sand Sheet.

once endorheic (closed basin fluvial systems) as opposed to exorheic systems that would lead to a sea or ocean. As an example, we discuss the morphology of the radar rivers constituting the sub-surface land-locked drainage system in the Great Salima Sand Sheet. Well-defined channels and high drainage density of radar rivers indicate pronounced water erosion on the steepest slopes in the upper reaches of the system as seen in NW Sudan (Figure 5). In the middle reaches of a given river system, the valley, enlarged by floods, becomes wide enough to be associated with large volumes of alluvium. These flood plains appear as wide dark bands in the radar images (Figure 5). In the lower reaches, the valley is so wide that the traction force decreases and the deposits become finer. This part of the drainage system has the youngest braided channels superimposed (Figure 5).

When the water reaches an inland depression like the Great Salima Sand Sheet, it would initially form a lake (EL-Baz and Robinson, 1997; Robinson et al., in press). Over time, much of the lake water would seep into the underlying rocks to be stored as groundwater (El-Baz, 1988; El-Baz and Robinson, 1997), either in shallow unconfined to semi-confined aquifers, or in deeper fractured bedrock aquifers. Evaporation of the surface water produces playa deposits, observed in many trenches dug through the sand of the eastern Sahara as well as on the surface (El-Baz et al., submitted). After the climate changed and dry conditions prevailed, the wind began to rework the sand into dunes and sand sheets.

Evolution of the Nile in Nubia

In northern Sudan and southern Egypt (Nubia) the Nile forms a great bend, first flowing north from Khartoum, then SW for over 300 km before it resumes its northward course (Plate 1; Figure 6A) where is called the Cataract Nile. Here, the Nile follows a contorted path through crystalline Precambrian basement rocks and Cretaceous sedimentary cover.

SIR-C/X-SAR images reveal how structures of different age control much of the course of the Nile in Nubia (Stern and Abdelsalam, 1996). Many of these structures are defined by subdued relief and could have been mapped by geologists on the ground. However, the vastness and harsh climate of Nubia have inhibited such studies. Other structures are covered by sand, and SIR-C/X-SAR images have revealed them for the first time. These images show two sets of structures controlling the Cataract Nile: (1) NNW-trending strike-slip shear zones, such as those coinciding with the Keraf suture (Abdelsalam and Stern, 1996; Abdelsalam et al., 1998) (Figure 6B); these formed about 600 Ma and strongly control the river along the third and fifth cataract (Figures 6B and 6C); and (2) E-W steep, normal or strike-slip faults of late Cretaceous or younger age, common along the third cataract (Figure 6B).

A recent change in the river's course is demonstrated by a paleo-channel, 25 km long, lying as much as 10 km north of the Nile (Figure 6D). This indicates that the Nile along the fourth cataract has recently shifted to the south (Stern and Abdelsalam, 1996). The Nile at the fifth cataract follows structures associated with the Keraf suture (Figure 6B). These structures continue north of Abu Hamed, yet the Nile turns SW to form the Great Bend (Figure 6A). This deflection is probably due to recent uplift of the Nubian Swell (Stern and Abdelsalam, 1996) as Late Cenozoic E-W faults in northern Sudan and southern Egypt indicate. Before uplift of the Nubian Swell, the drainage now flowing along the fifth cataract may have continued north through what is now Wadi Gabgaba (Figure 6A). Quaternary uplift diverted the Nile to the SW, through the fourth cataract, perhaps to join a tributary of the Nile to the west (Stern and Abdelsalam, 1996).
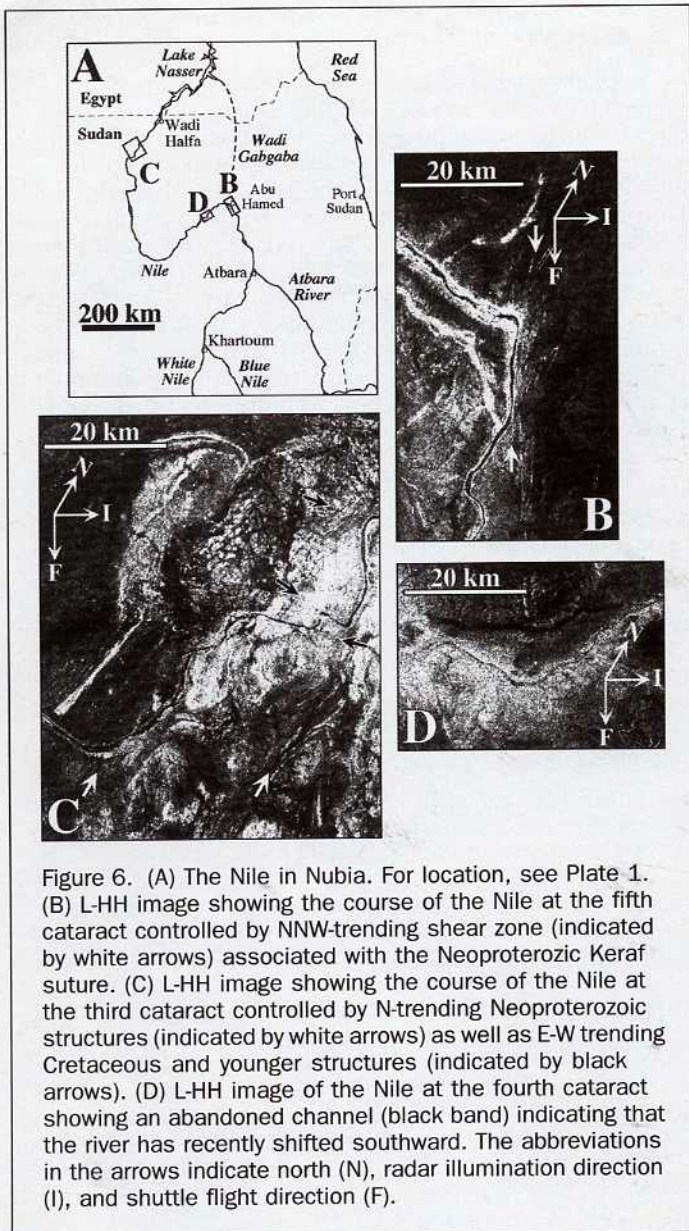
Figure 6. (A) The Nile in Nubia. For location, see Plate 1. (B) L-HH image showing the course of the Nile at the fifth cataract controlled by NNW-trending shear zone (indicated by white arrows) associated with the Neoproterozic Keraf suture. (C) L-HH image showing the course of the Nile at the third cataract controlled by N-trending Neoproterozoic structures (indicated by white arrows) as well as E-W trending Cretaceous and younger structures (indicated by black arrows). (D) L-HH image of the Nile at the fourth cataract showing an abandoned channel (black band) indicating that the river has recently shifted southward. The abbreviations in the arrows indicate north (N), radar illumination direction (I), and shuttle flight direction (F).
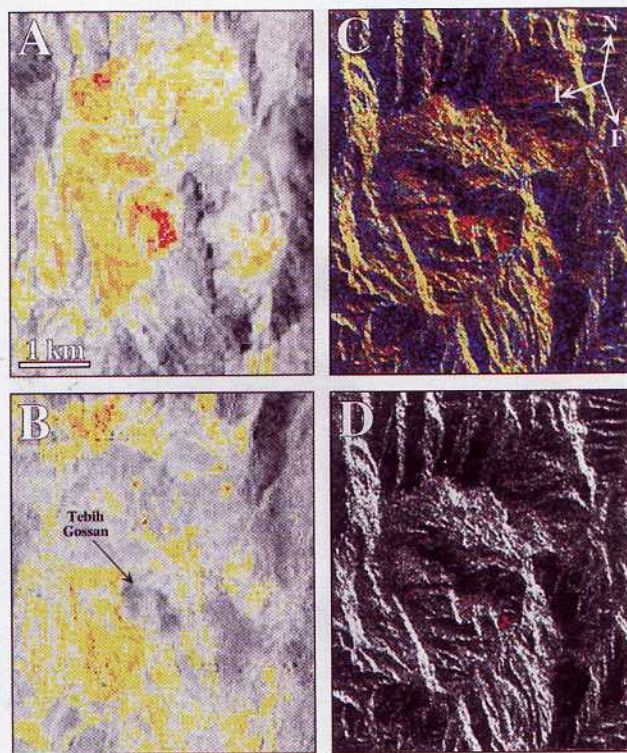

Plate 2. Images of the Tebih gossan in northern Eritrea (A) Iron index map draped over 3/1 Landsat TM image. (B) Clay index map draped over 5/7 Landsat TM image. The red color indicates density slicing at top 5 percent of the digital number (DN) of the ratio image, orange indicates top 10 percent, and yellow indicates top 15 percent. These images show the Tebih gossan have high iron but no clay alteration (C) C-HH, L-HH, L-HH/C-HH SIR-C/X-SAR image showing the Tebih gossan as characteristically red due to back-scattering enhancement of the C band. (D) Results of parallelepiped supervised classification based on L-HH, L-HV, C-HH, and C-HV bands draped over C-HH SIR-C/X-SAR image. These results confirm the visibility of the Tebih gossan in the radar image.

Mineral Exploration

We discuss the usefulness of orbital imaging radar for (1) direct identification of mineral deposits, specifically massive sulfide deposits of the Beddaho alteration zone in northern Eritrea (Plate 1), and (2) understanding geologic controls on mineral deposits.

Direct Detection

Massive sulfide deposits in the Nubian Shield in the eastern Sahara have surface expression in the form of hydrothermally altered zones containing distinctive clay and iron minerals. These sometimes enclose bodies in which iron-oxide minerals concentrate to form rough crusts referred to as gossans. Gossans have rough surfaces compared to the surrounding hydrothermally altered supracrustal rocks, hence, can be distinguished with SIR-C/X-SARimages. This is true for the Tebih gossan that comprises part of the Beddaho alteration zone in northern Eritrea (Abdelsalam et al., submitted) (Plate 2).

The iron (A in Plate 2) and clay (B in Plate 2) alteration index maps produced from band-ratios 3/1 and 5/7 Landsat TM images reveal the Tebih gossan as a horseshoe-shaped structure with high iron concentration and lacking clay alteration as would be expected. Comparing iron and clay alteration index maps with the SIR-C/X-SAR image (C in Plate 2) confirms the visibility of the Tebih gossan in the latter (D in Plate 2) where the bright appearance is due to enhancement of backscattering of the radar signal by the gossan's rough surfaces (Abdelsalam et al., submitted) and probably secondary dielectric effects because of iron enrichment.

Geologic Controls

Orbital imaging radar data have been integrated with Landsat TM images and geophysical data to understand lithological and structural controls on ore bodies (Rheault et al., 1989; Harris et al., 1989; Rowan and Bowers, 1995). This is useful in understanding the regional distribution of ore deposits and their geologic controls, given the importance of orbital imaging radar for lithological and structural mapping in the eastern Sahara.

Discussion and Conclusion

Application of orbital imaging radar for geologic studies in the eastern Sahara results in significant advances of geologic knowledge of the region.

- It is not generally possible to directly identify rock types with orbital imaging radar. These images can however be useful in lithological mapping if various rock types have different surface roughness due to varying susceptibility to weathering. Different surface roughness result in intensity variation of backscattering manifested by various tones on the radar images. Hence, the tone (controlled by microscale roughness (Lewis *et al.*, 1988)) and texture (controlled by mesoscopic and macroscale roughness (Lewis *et al.*, 1988)) in the SIR-C/X-SAR images can be used to distinguish between different rock types. Farr and Chadwick (1996) used this approach to map alluvial fan deposits of different ages in the Kun Lun Mountains of China. Similarly, radar images were used to map volcanic flows of different ages because older flows have smoother surfaces compared to younger ones (Zebker *et al.*, 1996). Results from the eastern Sahara extend the application of orbital imaging radar for lithological mapping.
- In the eastern Sahara, Neoproterozoic ductile structures such as folds and shear zones are defined by the trends of alternating lithological units. Neoproterozoic brittle structures instead are defined by truncation of layering (Figure 2). Hence, both types are lithologically defined structures. Orbital imaging radar is not as useful as orbital VNIR images in mapping lithologies and lithologically defined structures. However, in areas with low-lying relief, the morphology often follows lithological layering. This produces mesoscale roughness that is manifested as textural difference in radar images. In this case, orbital imaging radar is superior to orbital VNIR images in structural mapping where lithologic variations appear as subtle textural differences on the latter (Figure 2). Cretaceous and younger structures in the eastern Sahara Desert, on the other hand, deform both Neoproterozoic crystalline basement rocks and Cretaceous and younger cover. They are dominantly brittle and defined by morphological features such as escarpments, cliffs, and silicified ridges. Orbital radar is effective in imaging these because of radar double-bounce, normal-reflection, and edge-effect. These structures are best imaged by orbital radar when they are oriented at a high angle to the radar look direction. In areas with subdued relief, however, edge-effect dominates because outcrops are too low-lying to cause radar double-bounce and normal-reflection (Figure 2). However, in these areas, backscattering interferes with edge-effect at steep (more than 30°) radar look angles. At low radar look angles (less than 30°), the perceived roughness level decreases and normal-reflection and edge-effect dominate. This allows imaging of low-lying topographic features such as fault scarps that are hard to detect on orbital VNIR images. For example, the San Andreas Fault is invisible in VNIR images over part of its length, but is clearly delineated by radar images (Sabins *et al.*, 1980). This becomes important in the eastern Sahara for delineating potential areas with ground-water resources by defining fracture bedrock aquifers (Bisson and El-Baz, 1991).
- Orbital imaging radar has become increasingly important in mapping geomorphological features in arid regions such as the eastern Sahara. Images of sub-surface features buried under the sand of the eastern Sahara have been important for a number of geomorphological studies (Berlin *et al.*, 1985; Berlin *et al.*, 1986; McCauley *et al.*, 1986a; McCauley *et al.*, 1986b; El-Baz, 1988; Stern and Abdelsalam, 1996 EL-Baz and Robinson, 1997). Low-lying morphological features are imaged by orbital radar better than by orbital VNIR images because of radar side-looking geometry. Sand dunes and surface paleo-drainage are best imaged with radar look angles smaller than 30° because this allows normal-reflection and edge-effect to dominate over penetration. On the other hand, sub-surface geomorphological features are best imaged when the radar look angle is greater than 30°. Based on orbital radar images alone, however, it is difficult to determine whether the imaged feature is exposed on the surface or buried under sand. Hence, it is important to compare radar with VNIR images in order to determine whether the imaged feature is surface or sub-surface.
- Orbital imaging radar is not widely used for mineral exploration. This is because, unlike VNIR data, radar does not measure spectral features directly related to the mineralogy of geologic material. SIR-C/X-SAR data were successfully used to image the Tebih gossan in northern Eritrea because of its surface roughness. This, however, might not be applied for other mineral deposits in the eastern Sahara. Nevertheless, the orbital imaging radar has been used to understand geologic controls of mineral deposits.

Orbital imaging radar has tremendous advantages in imaging the eastern Sahara over VNIR images. It can be especially useful in outlining regional geologic and geomorphologic features. The SIR-C/X-SAR data are experimental and do not have complete coverage of the Earth's surface. Nevertheless, these data have been used by us and other scientists in important studies in the eastern Sahara. Moreover, SRTM data will cover the Earth's surface between 60°N and 54°S with C-HH radar data (Table 1). These data will provide relatively inexpensive orbital radar images to explore the entire eastern Sahara as well as producing high-resolution (30-m) digital elevation models (DEM). Other orbital radar systems also promise to contribute significantly towards better understanding of the eastern Sahara.

Acknowledgments

References

Abdelsalam, M.G., R.J. Stern, H. Schandelmeier, and M. Sultan, 1995. Deformational history of the Neoproterozoic Keraf Zone in NE Sudan, revealed by Shuttle Imaging Radar, *Journal of Geology*, 103:475–491.

Abdelsalam, M.G., and R.J. Stern, 1996. Mapping Precambrian structures in the Sahara Desert with SIR-C/X-SAR Radar: The Neoproterozoic Keraf Suture, NE Sudan, *Journal of Geophysical Research*, 101:23,063–23,076.

Abdelsalam, M.G., R.J. Stern, P. Copeland, E.M. Elfaki, B. Elhur, and F.M. Ibrahim, 1998. The Neoproterozoic Keraf Suture in NE Sudan: Sinistral transpression along the eastern margin of west Gondwana, *Journal of Geology*, 106:133–147.

Abdelsalam, M.G., R.J. Stern, and W.G. Berhane, submitted. Mapping gossans in arid regions with Landsat TM and SIR-C/X-SAR imagery: The Beddaho alteration zone in northern Eritrea, *Journal of African Earth Sciences*.

Askene, J.M, M. Lepparanta, and T. Thompson, 1992. The Bothnian experiment in preparation for ERS-1, 1988 (BEPERS-88) - An overview, *International Journal of Remote Sensing*, 13(13):2377–2398.

Barrat, J.A., S. Fourcade, B.M. Jahn, J.L. Cheminee, and R. Capdevila, 1998. Isotope (Sr, Nd, Pb, O) and trace-element geochemistry of volcanics from the Erta Ale range (Ethiopia), *Journal of Volcanology and Geothermal Research*, 80:85–100.

Barth, H., C. Besang, H. Lenz, and K-H. Meinhod, 1983. Results of Petrological Investigations and Rb/Sr age determinations on the Non-orogenic Igneous Ring Complexes in the Bayuda Desert, Sudan, *Geologisches Jahrbuch*, 51:3–34.

Berberi, F., H. Tazieff, and J. Varet, 1972. Volcanism in the Afar Depression: Its tectonic and magnetic significance, *Tectonophysics*, 15:19–29.

Berckhemer, H., B. Baier, H. Bartelson, A. Behle, H. Burkhardt, H. Gebrande, J. Makris, H. Henzel, H. Miller, and R. Vees, 1975. Deep seismic sounding in the Afar region and on the highland of Ethiopia, *Afar Between Continent and Oceanic Rifting* (A. Pilger and A. Rosler, editors), Schweizerbart, Stuttgart, pp. 89–107.

Berlin, G.L., M.A. Tarabzouni, K.M. Sheikho, and A. Al-Nasser, 1985. SIR-A and Landsat MSS observations of eolian sand and deposits on the Al Labbah Plateau, Saudi Arabia, *Proceedings of the Nineteenth International Symposium on Remote Sensing of Environment*, Ann Arbor, Michigan, pp. 311–321.

Berlin, G.L., M.A. Tarabzouni, A. Al-Nasser, K.M. Sheikho, and R.W. Larson, 1986. SIR-B sub-surface imaging of a sand-buried landscape: Al Labbah Plateau, Saudi Arabia, *IEEE Transactions of Geoscientific Remote Sensing*, 24:595–602.

Bisson, R.A., and F. El-Baz, 1991. Megawatersheds exploration model, *Proceedings of the Twentythird International Symposium on Remote Sensing of Environment*, Ann Arbor, Michigan, pp. 247–273.

Blom, R.G., R.E. Crippen, and C. Elachi, 1984. Detection of subsurface features in SEASAT radar images of Means Valley, Mojave Desert, California, *Geology*, 12:346–349.

Born, G.H., J.A. Dunne, and D.B. Lane, 1979. SEASAT mission overview, *Science*, 204:1405–1406.

Campbell, M.J., and J. Ulrichs, 1969. Electrical properties and their significance for lunar radar observations, *Journal of Geophysical Research*, 74:5867–5881.

Campbell, B.A., and D.B. Campbell, 1992. Analysis of volcanic surface morphology on Venus from comparison of Arecibo, Magellan, and terrestrial airborne radar data, *Journal of Geophysical Research*, 97:16293–16314.

Cimino, J.B., and C. Elachi, 1982. *Shuttle Imaging Radar - A (SIR-A) Experiment*, Jet Propulsion Laboratory Publication 82-77, Pasadena, California, 650 p.

Earth Observation Center, National Space Development Agency of Japan, 1999. *PALSAR*, URL: *http://eoc.nasda.go.jp/guide/satellite/sendata/palsar j.html*.

Elachi, C., 1981. Earth observation with the SEASAT spaceborne imaging radar: An introduction, *Photo Interpretation*, 20(4):2–3.

———, 1984. *The SIR-B Science Investigation Plan*, Jet Propulsion Laboratory Publication 84–3, Pasadena, California, 197 p.

———, 1986. *The Second Spaceborne Imaging Radar Symposium*, Jet Propulsion Laboratory Publication 86–26, Pasadena, California, 223 p.

Elachi, C., and J. Granger, 1982. Spaceborne imaging radars probe 'in depth,' *IEEE Spectrum*, 19:24–29.

Elachi, C., L.E. Roth, and G.G. Schaber, 1984. Spaceborne radar subsurface imaging in hyper-arid regions, *IEEE Transactions of Geoscientific Remote Sensing*, 22:383–388.

El-Baz, F., 1988. Origin and evolution of the desert, *Interdisciplinary Science Reviews*, 13:331–347.

El-Baz, F., and C.A. Robinson, 1997. Paleo-channels revealed by SIR-C data in the Western Desert of Egypt: Implications to sand dune accumulations, *Proceedings of the Twelfth International Conference on Applied Geologic Remote Sensing*, Ann Arbor, Michigan, pp. 469–476.

El-Baz, F., C.A. Robinson, M.M. Mainguet, M. Said, M. Nabih, H.I. Himida, and H.A. El-Etr, submitted. Distribution and morphologies of paleo-channels in southwest Egypt and northwest Sudan, *Palaeoecology of Africa*.

European Space Agency, 1998. *ENVISAT-1*, URL: *http://envisat.estec.esa.nl/*.

Evans, D.L., and J.J. Plaut, 1996. *Science Results from the Spaceborne Imaging Radar-C/X-Band Synthetic Aperture Radar (SIR-C/X-SAR): Progress Report*, Jet Propulsion Laboratory Publication 96-7, Pasadena, California, 265 p.

Farr, T.G., and O.A. Chadwick, 1996. Geomorphic processes and remote sensing signatures of alluvial fans in the Kun Lun Mountains, China, *Journal of Geophysical Research*, 101:23,091–23,100.

Farr, T.G., and M. Kobrick, 1998. The Shuttle Radar Topography Mission: A global DEM, *The Geological Society of America Annual Meetings Abstracts with Programs*, 30:359.

Femenias-Pierre, M.A., 1998. ERS-2 radar altimeter: 3 years of results, *Annales Geophysicae*, 16(1):247.

Ford, J.P., R.G. Blom, J.A. Crisp, C. Elachi, T.G. Farr, R.S. Saunders, E.E. Theilig, S.D. Wall, and S.B. Yewell, 1989. *Spaceborne Radar Observations: A Guide for Magellan Radar-Image Analysis*, Jet Propulsion Laboratory Publication 89–4, Pasadena, California, 126 p.

Ford, J.P., J.B. Cimino, and C. Elachi, 1983. *Space Shuttle Columbia Views the World with Imaging Radar: The SIR-A Experiment*, Jet Propulsion Laboratory Publication 82–95, Pasadena, California, 179 p.

Ford, J.P., J.B. Cimino, B. Holt, and M. Rusek, 1986. *Shuttle Imaging Radar Views the Earth from Challenger: The SIR-B Experiemnt*, Jet Propulsion Laboratory Publication 82–95, Pasadena, California, 179 p.

Fu, L.L., and B. Holt, 1982. *Seasat Views Oceans and Sea Ice with Synthetic Aperture Radar*, Jet Propulsion Laboratory Publication 81-120, Pasadena, California, 200 p.

Harris, J., 1989. Data integration for gold exploration in eastern Nova Scotia using a GIS, *Proceedings of the Seventh Thematic Conference in Remote Sensing Exploration Geology*, Calgary, Alberta, Canada, pp. 233–250.

Hayward, N.J., and C.J. Ebinger, 1996. Variations in the along-axis segmentation of the Afar Rift system, *Tectonics*, 15:244–257.

Hoekstra, P.A., and [X.X.] Delaney, 1974. Dieletric properties of soils at UHF and microwave frequencies, *Journal of Geophysical Research*, 79:1699–1708.

Jordan, R.L., B.L. Huneycutt, and M. Werner, 1995. The SIR-C/X-SAR Synthetic Aperture Radar System, *IEEE Transactions of Geoscientific Remote Sensing*, 33:829–839.

Kobrick, M., 1985. *SIR-B Report*, Jet Propulsion Laboratory Publication 85–7, Pasadena, California, pp. 11–16.

Koopmans, B.N., 1991. The first ERS-1 SAR image over the Netherlands: An appraisal for off-shore areas, *Geocarto International*, 6(4):39–43

Lewis, A.J., F.M. Henderson, and D.W. Holcomb, 1998. Radar fundamentals: the Geoscience prospective, *Principals and Applications of Imaging Radar* (F.M. Henderson and A.J. Lewis, editors), John Wiley and Sons, New York, pp. 131–181.

McCauley, J.F., G.G. Schaber, C.S. Breed, M.J. Grolier, C.V. Haynes, B. Issawi, C. Elachi, and R. Blom, 1982. Sub-surface valleys and geoarcheology of the Eastern Sahara revealed by shuttle radar, *Science*, 218:1004–1020.

McCauley, J.F., C.S. Breed, G.G. Schaber, W.P. McHugh, B. Issawi, C.V. Haynes, M.J. Grolier, and A.E. Kilani, 1986a. Paleodrainage of the Eastern Sahara - The radar rivers revisited, *IEEE Transactions of Geoscientific Remote Sensing*, 24:624–648.

McCauley, J.F., C.S. Breed, and G.G. Schaber, 1986b. The megageomorphology of the radar rivers of the eastern Sahara, *The Second Spaceborne Imaging Radar Symposium*, 28-30 April, Jet Propulsion Laboratory Publication 86–26, Pasadena, California, pp. 25–35.

McKenzie, D.P., D. Davies, and P. Molnar, 1970. Plate tectonics of the Red Sea and East Africa, *Nature*, 226:243–248.

Mohr, P.A., 1983. Ethiopian flood basalt provice, *Nature*, 303:577–584.

Moon, W.M., Bo. Li, J.S. Won, H.W. Yoo, V. Singhroy, and Y. Yamaguchi, 1994. JERS-1 SAR data characteristics for geological applications, *Collected Reprints, KORDI Research Papers*, 11:1077–1086.

Okonek, S., 1999. *SRTM home page*, URL: *http://www-radar.jpl.nasa.gov/srtm/*.

Oppenheimer, C., and P. Francis, 1998. Implications of longlived lava lakes for geomorphological and plutonic processes at Erta Ale volcano, Afar, *Journal of Volcanology and Geothermal Research*, 80:101–111.

Parashar, S., E. Langham, J. McNally, and S. Ahmed, 1993. RADARSAT mission requirements and concepts, *Canadian Journal of Remote Sensing*, 19:280–288.

Raisz, E., 1952. *Landform Map of North Africa (1:5,000,000)*, Environmental Protection Branch, Quartermaster General, U.S. Army.

Robinson, C.A., F. El-Baz, and V. Singhroy, in press. Subsurface imaging by Radarsat: Comparison with Landsat TM Data and implications to ground water in the Selima area, Northwestern Sudan, *Canadian Journal of Remote Sensing*.

Roth, L.E., and C. Elachi, 1975. Coherent electromagnetic losses by scattering from volume inhomogeneities, *IEEE Transactions of Antennas and Propagation*, 23:674–675.

Rheault, M., R. Simard, C. Garneau, and V.R. Slaney, 1989. SAR Landsat TM-geophysical data integration utility of value-added products in geological exploration, *Proceedings of the Seventh Thematic Conference on Remote Sensing of Exploration Geology*, Calgary, Alberta, pp. 549–559.

Rowan, L.C., and Bowers, T.L. 1995. Analysis of linear features mapped

in Landsat Thematic Mapper and side-looking airborne radar images of the Reno 1° by 2° quadrangle, Nevada and California: Implication for mineral resource studies, *Photogrammetric Engineering & Remote Sensing*, 61:749–759.

Sabins, F.F., 1997. *Remote Sensing Principles and Interpretation*, W.H. Freeman and Company, New York, 494 p.

Sabins, F.F., R. Blom, and C. Elachi, 1980. Seasat radar image of the San Andreas fault, California, *American Association of Petroleum Geologists Bulletin*, 64:619–628.

Sandford, K.S., 1949. Notes on the Nile Valley in Berber and Dongola, *Geological Magazine* , 86:97–109.

Schaber, G.G., J.F. McCauley, and C.S. Breed, 1997. The use of multi-frequency and polarimetric SIR-C/X-SAR data in geologic studies of Bir Safsaf, Egypt, *Remote Sensing of Environment*, 59:337–363.

Schoonmaker, J.W., Jr., 1997. *An Overview of LightSAR: A Proposed Radar Satellite*, United States Geological Survey Open File Report OF 98–0031, 72p.

Schreier, G., K. Maeda, and B. Guindon, 1991. Three spaceborne SAR sensors: ERS-1, J-ERS-1 and RADARSAT: Competition or synergism? *Geo Informations Systeme*, 4(2):20–27.

Stern, R.J., and M.G. Abdelsalam, 1996. The origin of the great bend of the Nile from SIR-C/X-SAR imagery, *Science*, 274:1696–1698.

Szabo, B.J., C.V. Haynes, and T.A. Maxwell, 1995. Ages of Quaternary pluvial episodes determined by Uranium-series and radiocarbon dating of lacustrine deposits of Eastern Sahara, *Paleogeography, Paleoclimatology, Paleoecology*, 113:227–242.

Yelizavetin, I.V., 1992. Digital simulation of surface relief using stereoradar data from the "Almaz-1" satellite, *Issledovaniye Zemli iz Kosmosa*, 6:53–61.

Zebker, H.A., and R.M. Goldstein, 1986. Topographic mapping from interferometric synthetic aperture radar observations, *Journal of Geophysical Research*, 9:4993–4999.

Zebker, H.A., P. Rosen, S. Hensley, and P.J. Mouginis-Mark, 1996. Analysis of active lava flows on Kilauea volcano, Hawaii, using SIR-C radar correlation measurements, *Geology*, 24:495–498.